Carburisation of ferritic Fe-Cr alloys by low carbon activity gases

Thomas Gheno, Daniel Monceau, Jianqiang Zhang, David J. Young

Carburisation of ferritic Fe–Cr alloys by low carbon activity gases

Thomas Gheno [a,b], Daniel Monceau [b], Jianqiang Zhang [a], David J. Young [a,*]

[a] School of Materials Science and Engineering, The University of New South Wales, Sydney, NSW 2052, Australia
[b] Institute Carnot CIRIMAT, ENSIACET, 31030 Toulouse Cedex 4, France

A B S T R A C T

Model Fe–Cr alloys were exposed to Ar–CO_2–H_2O gas mixtures at 650 and 800 °C. At equilibrium, these atmospheres are oxidising to the alloys, but decarburising ($a_C \approx 10^{-15}$ to 10^{-13}). In addition to developing external oxide scales, however, the alloys also carburised. Carbon supersaturation at the scale/alloy interface relative to the gas reflects local equilibrium: a low oxygen potential corresponds to a high p_{CO}/p_{CO_2} ratio, and hence to a high carbon activity. Interfacial carbon activities calculated on the basis of scale–alloy equilibrium are shown to be in good agreement with measured carburisation rates and precipitate volume fractions, providing support for the validity of the thermodynamic model.

Keywords:
A. Steel
C. Carburisation
C. High temperature corrosion
C. Oxidation

1. Introduction

Materials to contain and convey hot gases rich in CO_2 are needed in various carbon capture technologies currently being developed. The process gases concerned are expected from their composition (principally CO_2 plus H_2O) to induce oxidation, but seem to pose no threat to conventional materials in terms of carburisation. For instance, pure CO_2 equilibrated at atmospheric pressure and a temperature of 650 °C corresponds to $p_{O_2} = 1.5 \times 10^{-8}$ atm and $a_C = 2.7 \times 10^{-15}$. Nonetheless, available information indicates that heat resisting alloys can also be attacked by carbon in these gases.

The oxygen partial pressure of CO_2 gas is high enough for iron to oxidise, and dilute Fe–Cr alloys readily form Fe-rich oxide scales upon exposure to CO_2 at high temperatures. In addition, carburisation of the underlying substrate has been reported by several authors. Internal carbides were observed after exposure of 9Cr (P92) and 12Cr (X20 and VM12) steels to Ar–50%CO_2 at 550 °C [1], and after exposure of model Fe–Cr alloys to Ar–30%CO_2 at 650 °C [2]. Reaction of pure CO_2 with an 18Cr (304) steel at 704, 816 and 927 °C [3] and with an Fe–15Cr alloy at 900 °C [4] also led to internal carbide precipitation. Fujii and Meussner [5] reported simultaneous oxidation and carburisation of Fe–Cr alloys containing 1–15 wt.% Cr in pure CO_2 at temperatures of 700, 900 and 1100 °C. All alloys remained ferritic at 700 °C and produced (Fe,Cr) carbides, the nature of which varied with alloy chromium content from $(Fe,Cr)_3C$ to $(Fe,Cr)_7C_3$ and $(Fe,Cr)_{23}C_6$, in accordance with the Fe–Cr–C phase diagram. Carbon-containing austenite was formed at the higher temperatures and produced ferrite plus pearlite, martensite and/or (Fe,Cr) carbides upon cooling to room temperature, according to the alloy chromium content.

Clearly, the equilibrium carbon activity of the bulk gas phase is insufficient to form the carburisation products reported. McCoy [3] suggested that oxide formation from direct reaction of iron with CO_2 could generate CO,

$$Fe(s) + CO_2(g) = FeO(s) + CO(g) \quad (1)$$

which would then build up in pores within the oxide, causing the local carburising potential to increase. Fujii and Meussner [5] proposed that carbon was generated on the oxide surface, transported through a dense outer oxide layer and produced a CO–CO_2 atmosphere within voids in a porous inner oxide layer. However, subsequent experiments [6] showed that the solubility of carbon in iron oxides is extremely small, and its solid-state diffusion through iron oxide scales is not feasible. Transport could occur instead by means of molecular CO_2, but the scale microstructures are reported [5] to appear impermeable to gas. Furthermore, these scales grow at rates controlled by solid-state diffusion, and continuous pathways for gas phase transport through the scale therefore cannot exist during steady-state oxidation. In more recent studies involving carburisation of chromia-forming materials [7–9], molecular transport via grain boundaries has been suggested to account for carbon transfer through the scale.

Several descriptions [1,2,10,11], which are thermodynamically equivalent but mechanistically different, have been proposed to account for the generation of a carburising environment within the scale. In reference [10], local equilibrium is represented by the reactions

* Corresponding author. Tel.: +61 2 9385 4322; fax: +61 2 9385 5956.
E-mail address: d.young@unsw.edu.au (D.J. Young).

doi:10.1016/j.corsci.2011.05.013

$$CO_2 = CO + \frac{1}{2}O_2 \quad (2)$$

$$2CO = CO_2 + C \quad (3)$$

At the scale/alloy interface, the oxygen potential is kept to a low value, $(p_{O_2})_{eq}$, by the metal–oxide equilibrium,

$$M + \frac{y}{2}O_2 = MO_y \quad (4)$$

and might therefore lead to elevated carbon activities, as illustrated in Fig. 1.

Microstructural changes induced in steels by carburisation will affect their mechanical properties. This paper is concerned with determining the conditions leading to carburisation of model Fe–Cr alloys in CO_2, and understanding those conditions in terms of the thermodynamics of reactions (2) and (3). The effect of water vapour on carburisation is also explored.

2. Materials and experiments

Binary alloys were prepared by argon arc melting Fe (99.99% pure) and Cr (99.995% pure) to yield nominal compositions (wt.%): Fe–2.25Cr, Fe–9Cr and Fe–20Cr. Ingots were annealed in Ar–5%H_2 at 1150 °C for 48 h, and cut into rectangular samples of approximate dimensions 14 × 6 × 1.5 mm. As-annealed materials had microstructures of coarse-grained (≈500 μm) ferrite. The composition of an Fe–9Cr ingot was verified by chemical analysis. The chromium content was measured as (9.2 ± 0.3) wt.% by ICP-OES, and no carbon could be detected after combustion in a LECO CS230 instrument, with a 4 ppm sensitivity. Samples were mechanically ground to a 1200 grit finish, degreased and ultrasonically cleaned in ethanol before reaction.

Isothermal corrosion experiments were conducted at 650 and 800 °C in Ar–20%CO_2 and Ar–20%CO_2–20%H_2O mixtures at a total pressure of about 1 atm. Linear gas flow rates were set at about 2 cm s^{-1}. The wet gas was generated by passing a mixture of Ar and CO_2 through a thermostated water saturator. The demineralised water in contact with the gas mixture was set at 77 °C. Excess water vapour was subsequently condensed by cooling the wet gas in a distillation column at 60 °C.

Oxygen is formed by the decomposition of CO_2, reaction (2), and of H_2O

$$H_2O = H_2 + \frac{1}{2}O_2 \quad (5)$$

while carbon is produced by the Boudouard reaction, (3), and/or the syngas reaction

$$CO + H_2 = C + H_2O \quad (6)$$

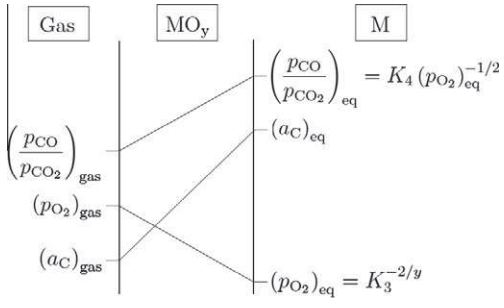

Fig. 1. Activities in a gas–MO_y–M system, where M is a pure metal. Equilibrium constants, K_i, and boundary values of partial pressures and activities are defined in text.

Equilibrium activities of oxygen and carbon calculated from standard free energies tabulated in Ref. [12] are given in Table 1. The values are such that all conditions are oxidising and decarburising to the alloys.

Reaction products were examined using X-ray diffraction (XRD), optical microscopy (OM), scanning electron microscopy combined with energy-dispersive X-ray analysis (SEM-EDX), and transmission electron microscopy (TEM) together with EDX and selected area diffraction (SAD) analysis. Metallographic observations were carried out on polished and etched cross-sections. Etching with a solution of 1% picric acid and 5% hydrochloric acid in ethanol was used to reveal alloy grain boundaries and internal carbides, and to distinguish wustite from the spinel phase in oxide scales. Murakami's reagent (1 g $K_3Fe(CN)_6$ and 1 g KOH for 10 mL H_2O) was also employed for revealing carbides.

3. Results

3.1. Formation of external oxide scales

Alloys containing 2.25 and 9 wt.% Cr formed thick, multi-layered oxide scales in dry and wet CO_2 at both 650 and 800 °C. The layers were identified by alternately grinding off some oxide and performing XRD measurements on the ground surface. The outer layers were iron oxides, while the inner layer consisted of a mixture of FeO and $(Fe,Cr)_3O_4$ spinel. Analysis by SEM-EDX confirmed the absence of chromium in the outer layers, and its presence in the inner layer. This structure, illustrated in Fig. 2, is typical of dilute Fe–Cr alloys and has been observed by others after exposure to CO_2 [5,13] and CO_2–H_2O [1,14] in the temperature range 550–900 °C.

Oxidation of the Fe–20Cr alloy was more sensitive to exposure conditions. When exposed to dry CO_2 at 650 °C, the alloy formed a thin Cr_2O_3 scale interrupted by nodules of iron-rich oxide (Fig. 3a). The surface area fraction covered by iron-rich oxide increased with reaction time, at least during early stages. In the wet gas, Cr_2O_3 was present only in small proportions for short reaction times, and the alloy mainly formed a continuous iron-rich scale. The iron-rich oxide was similar in structure to the oxide formed on dilute alloys (Fig. 2). At 800 °C, the alloy formed a continuous Cr_2O_3 scale in dry CO_2, but developed some iron-rich nodules in wet CO_2 (Fig. 3b).

Scale growth kinetics and morphologies will be discussed elsewhere. Attention is focused here on the alloy phase transformations accompanying corrosion.

3.2. Internal reactions at 650 °C

Exposure to dry CO_2 at 650 °C led to intergranular carburisation of the Fe–2.25Cr alloy. The precipitates shown in Fig. 4 were found throughout the whole sample after 120 h of reaction. No other internal reaction product was observed in this alloy.

In addition to an external scale, the Fe–9Cr alloy formed internal oxides and carbides (Fig. 5). The carbides were identified as $(Fe,Cr)_7C_3$ by grinding off the oxide scale and performing XRD measurements directly below the scale/alloy interface and deeper in

Table 1
Equilibrium oxygen and carbon potentials in the reacting gas at P = 1 atm.

T (°C)	Gas composition (%)			p_{O_2} (atm)	a_C
	Ar	CO_2	H_2O		
650	80	20	–	5.1×10^{-9}	1.6×10^{-15}
	60	20	20	1.1×10^{-8}	7.7×10^{-16}
800	80	20	–	1.6×10^{-7}	6.9×10^{-14}
	60	20	20	2.5×10^{-7}	4.2×10^{-14}

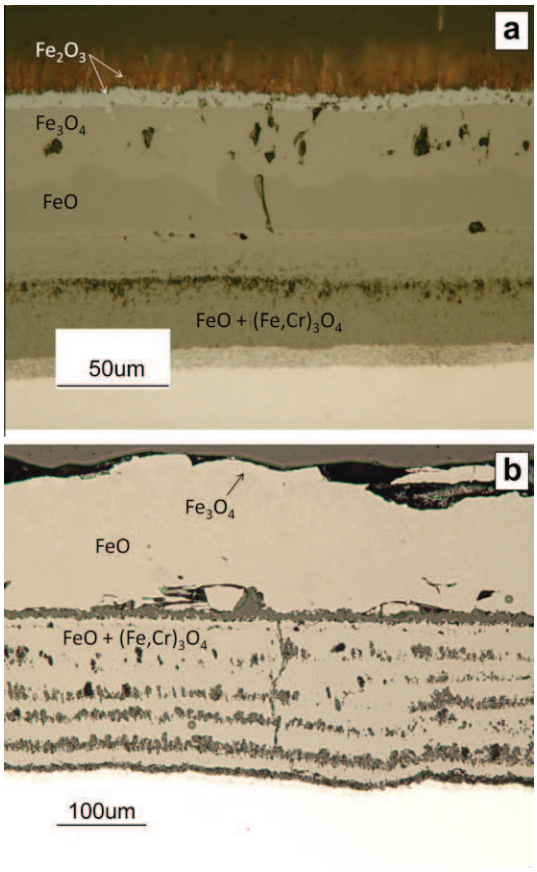

Fig. 2. External oxide scale formed on Fe–9Cr after (a) 120 h exposure to Ar–20CO_2 at 650 °C; (b) 30 h exposure to Ar–20CO_2–20H_2O at 800 °C.

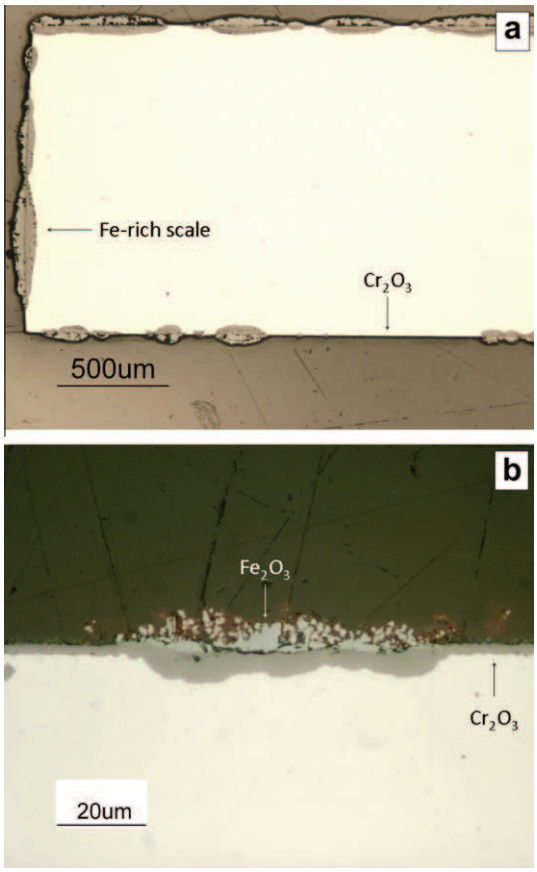

Fig. 3. External oxide scale formed on Fe–20Cr after (a) 120 h exposure to Ar–20CO_2 at 650 °C; (b) 100 h exposure to Ar–20CO_2–20H_2O at 800 °C.

the alloy (Fig. 6). Intragranular carbide penetration depths, X_C, were measured from the interface between internal oxidation and internal carburisation zones. In both dry and wet CO_2, X_C increased according to a parabolic law (Fig. 7)

$$X_C^2 = 2k_p t \tag{7}$$

where k_p is the rate constant. Carburisation is seen to be faster in the dry gas ($k_p = 6.5 \times 10^{-10}$ cm^2 s^{-1}) than in the wet gas ($k_p = 2.4 \times 10^{-10}$ cm^2 s^{-1}). Intergranular carbides were observed throughout the samples within a 40 h exposure to both atmospheres. The volume fraction of carbides in the ferrite matrix, f_V, was measured in 50 μm wide zones parallel to the surface using the ImageJ software, with a precision of around 2%. Results plotted against the relative depth are shown in Fig. 8. The profiles are similar for both gases, but the value at $x = 0$ is higher in the dry gas, with $f_V = 0.17$ compared with 0.14 in the wet gas.

Reaction of Fe–20Cr also led to internal oxidation and carburisation, but precipitate morphology and penetration depth varied with the nature of the overlaying oxide. Underneath the thin Cr_2O_3 scale, internal precipitation was absent or limited to a semi-connected array of intragranular carbides (Fig. 9a), with a relatively low penetration depth ($\leqslant$20 μm). Where the alloy formed an iron-rich oxide scale, internal reaction occurred to a larger extent, producing both small, equiaxed and elongated carbides (Fig. 9b). Both external scaling and internal precipitation varied considerably. Measurements of the extent of carburisation underneath the iron-rich scale were subject to substantial error, as seen from the error bars in the parabolic plots of Fig. 10. Carburisation rates in dry and wet CO_2 were similar, and the kinetics are therefore described with a common, average rate constant $k_p = (8 \pm 2) \times 10^{-11}$ cm^2 s^{-1}. Similarly, an average $f_V = 0.3$ was measured in near surface regions after exposure to both gases.

3.3. Internal reactions at 800 °C

At 800 °C, both Fe–2.25Cr and Fe–9Cr alloys underwent internal oxidation in addition to external scaling. No carburisation product could be observed in the Fe–2.25Cr alloy, whereas reaction of the Fe–9Cr alloy resulted in formation of carbides and martensite beneath the Fe-rich oxide scale (Fig. 11).

In the dry gas, intergranular carburisation of Fe–9Cr was fast, and occurred throughout the alloy within a 5 h exposure. Martensite was identified in etched cross-sections, visually (Fig. 11a) and by means of hardness testing. Vickers microhardness tests with a 200 g load yielded HV values of about 100 and 400 for ferrite and martensite, respectively. The extent of martensite formation increased with increasing reaction time. Although the phase transformation affected entire grains, it did not occur in a uniform manner along the metal/oxide interface: some grains neighbouring the martensite remained untransformed, while some isolated martensite was found deep inside the alloy, surrounded by untransformed grains.

In addition, internal carbides were occasionally observed in a narrow 10 μm strip between the internal oxidation zone and the martensite, as seen in Fig. 11. However, in other regions, no carbides were detected between the martensite and internal oxidation zone. Carbides were never detected in the absence of martensite, i.e. at the internal oxide/ferrite interface. Foil specimens were prepared from the sample shown in Fig. 11, by FIB milling. The TEM–EDS results in Fig. 12a and b reveal the matrix to be

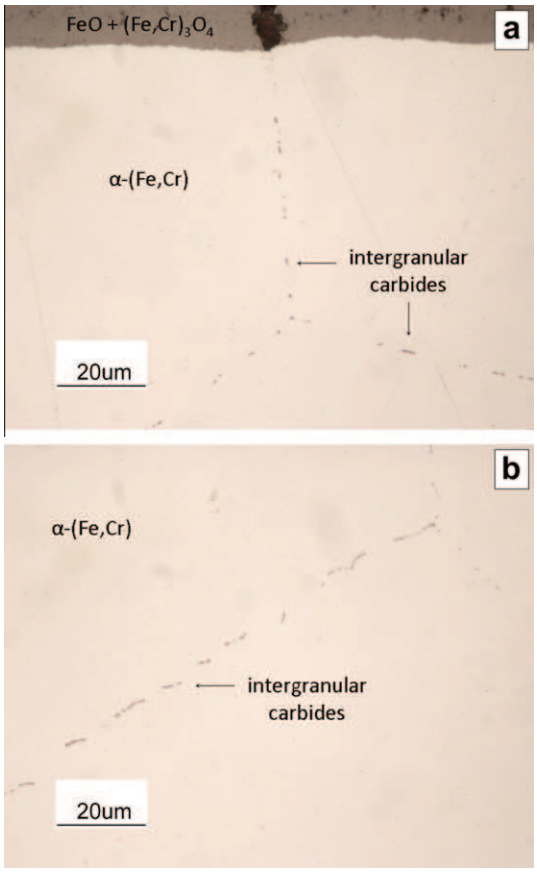

Fig. 4. Intergranular carburisation of Fe–2.25Cr after 120 h exposure to Ar–20CO_2 at 650 °C, etched with Murakami's reagent. (a) Scale/alloy interface; (b) deep within the alloy.

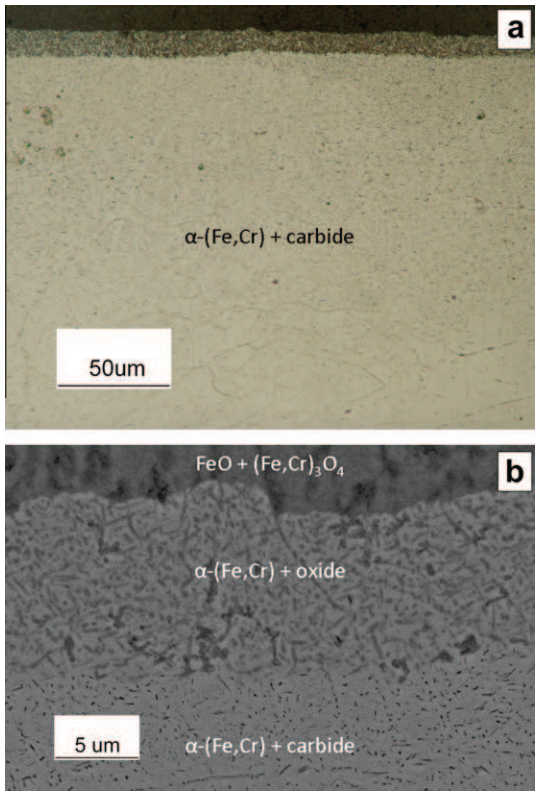

Fig. 5. Internal precipitation in Fe–9Cr after 120 h exposure to Ar–20CO_2 at 650 °C, etched with Murakami's reagent. (a) OM; (b) SEM, backscattered electrons.

depleted in chromium, and the carbides and oxides chromium-rich. Selected area diffraction patterns (SADP) were recorded and interpreted with the help of CaRIne Crystallography software [15]. Patterns shown in Fig. 12c and d fit well with α-Fe and $(Cr,Fe)_{23}C_6$, respectively. Fig. 13a and b show a bright field image and a SADP recorded from the martensite visible in Fig. 11a. The absence of cubic symmetry in the tetragonal structure allows the appearance of the $(2\bar{2}1)$ and $(2\bar{1}2)$ reflections, which are forbidden in ferrite.

In the wet gas, the Fe–9Cr alloy developed qualitatively similar carburisation products (martensite and carbides).

The Fe–20Cr alloy was less prone to internal reaction. No oxide and a very small number of elongated carbides (Fig. 14) were observed beneath the Cr_2O_3 scale.

4. Discussion

4.1. Activity of carbon at the metal/oxide interface

As noted in the Introduction, several mechanisms have been put forward to account for the carburisation of Fe–Cr alloys in low a_C, CO_2-rich atmospheres. However, a quantitative description of the carbon supersaturation developed in the alloy, relative to the gas, has been lacking.

Upon exposure to CO_2–H_2O mixtures, Fe–Cr alloys form oxide scales, and the conditions established within the scales might differ markedly from those prevailing in the gas [1,2,10,11]. Indeed, provided that the oxide scale is (i) sufficiently compact and adherent to constitute a physical barrier separating the metal from the

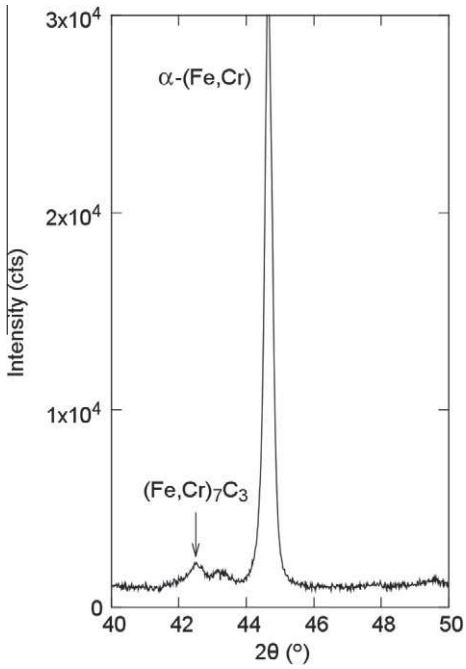

Fig. 6. XRD pattern recorded at about 40 μm below the metal/oxide interface of Fe–9Cr reacted 240 h at 650 °C.

atmosphere, and (ii) thick enough to be considered in local thermodynamic equilibrium, the oxygen activity within the scale varies between its ambient value at the oxide/gas interface, and the dissociation pressure of the oxide at the metal/oxide interface

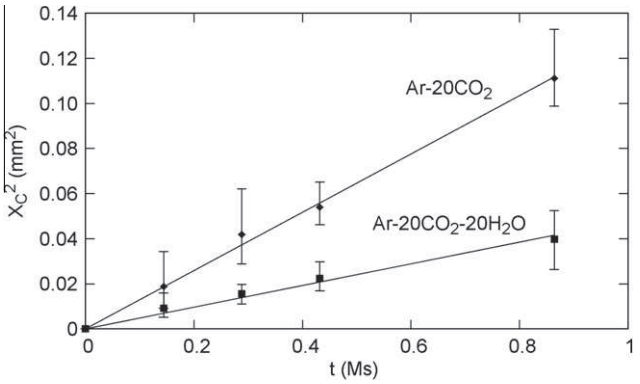

Fig. 7. Carburisation kinetics of Fe–9Cr at 650 °C. Values obtained from average of at least 10 measures, with minimum and maximum indicated by the error bars.

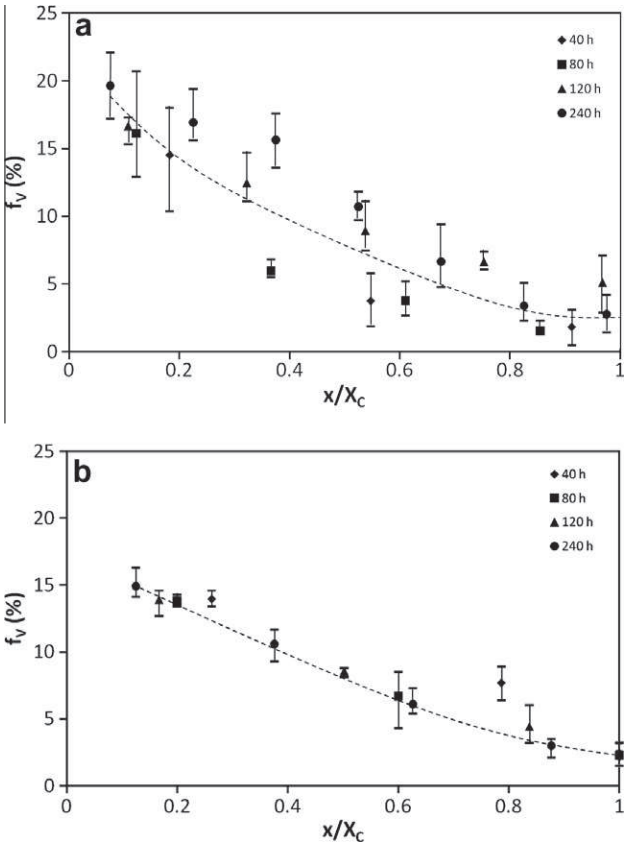

Fig. 8. Carbide volume fraction in Fe–9Cr exposed to (a) Ar–20CO_2 and (b) Ar–20CO_2–20H_2O at 650 °C. Values obtained from average of 4 measures at each depth, with minimum and maximum indicated by the error bars.

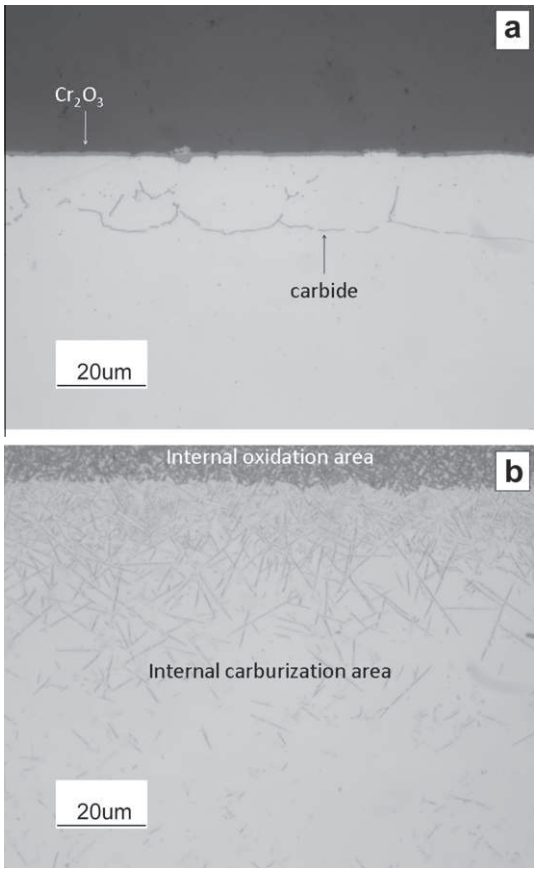

Fig. 9. Non-uniform carburisation pattern of Fe–20Cr after 120 h exposure to Ar–20CO_2 at 650 °C. Samples etched with Murakami's reagent. (a) Thin Cr_2O_3 scale and limited carburisation; (b) thick Fe-rich scale and extensive carburisation.

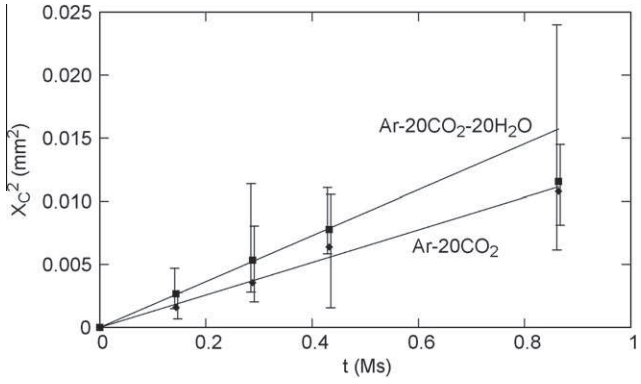

Fig. 10. Carburisation kinetics of Fe–20Cr at 650 °C. Values obtained from average of at least 10 measures, with minimum and maximum indicated by the error bars.

(see Fig. 1). If, in addition, the scale transmits the CO_2 and CO species, low values for p_{O_2} result in high values for p_{CO}/p_{CO_2} (by virtue of reaction (2)), and therefore for a_C (via reaction (3)). The phase constitution and composition of the growing scale control the establishment of chemical potential gradients and resulting driving forces, while its transport properties limit the availability of the molecular species at the metal/oxide interface.

It is proposed that all gas species but Ar can reach the scale/alloy interface, where local thermodynamic equilibrium is assumed to be achieved. Thus p_{O_2} is controlled by the metal/oxide equilibrium, and a_C set by the equilibrium of reactions (2) and (3). The p_{CO}/p_{CO_2} ratio can be expressed as a function of the dissociation pressure of the oxide, $(p_{O_2})_{eq}$

$$\frac{p_{CO}}{p_{CO_2}} = \frac{K_2}{(p_{O_2})_{eq}^{1/2}} \tag{8}$$

where K_2 is the equilibrium constant for reaction (2). This ratio depends only on the nature of the oxide, alloy composition and temperature.

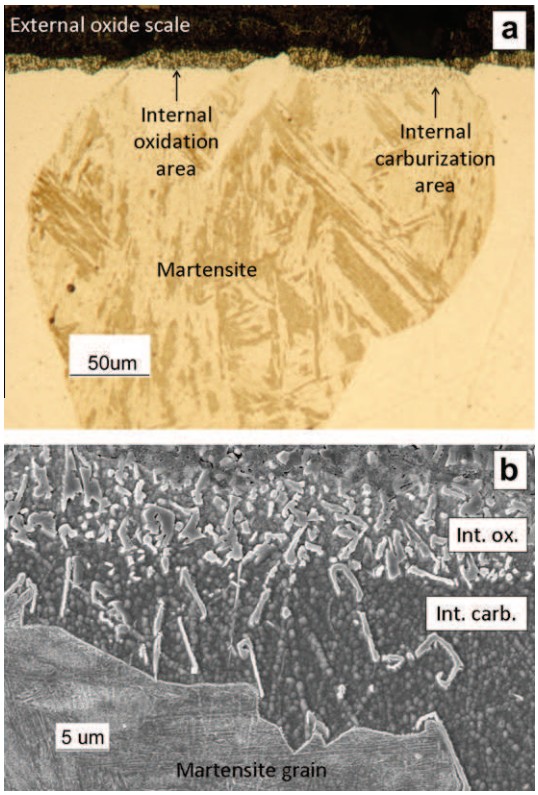

Fig. 11. Internal reaction products observed in Fe–9Cr after 20 h exposure to Ar–20CO_2 at 800 °C. Sample etched in picral + HCl. (a) Optical microscopy; (b) SEM.

The carbon activity can be determined from the Boudouard reaction equilibrium, as

$$a_C = K_3 \frac{p_{CO}^2}{p_{CO_2}} \tag{9}$$

Denoting by p_T the total pressure at the interface, and omitting the small p_{O_2} value, one obtains

$$p_T = p_{CO_2} + p_{CO} + p_{H_2O} + p_{H_2} \tag{10}$$

where again argon is assumed not to enter the scale. Eq. (9) can then be rewritten as

$$a_C = K_3 \frac{b^2 p_T}{(1+b)(1+\frac{\alpha}{\beta})} \tag{11}$$

where $b = p_{CO}/p_{CO_2}$, $\alpha = p_{H_2} + p_{H_2O}$ and $\beta = p_{CO} + p_{CO_2}$.

Describing the formation of carbon via the syngas reaction, (6), yields the same expression. According to Eq. (11), a_C is dependant upon two parameters: (i) p_T, which is a function of both the external pressure and the scale transport properties; and (ii) the $(p_{H_2} + p_{H_2O})/(p_{CO} + p_{CO_2})$ ratio. The latter is determined by its value in the reaction gas and the relative degree of uptake and transport of H-bearing and C-bearing molecules by the scale. The value of p_T is set at 0.2 atm for Ar–20CO_2 and 0.4 atm for Ar–20CO_2–20H_2O. In the absence of any data, hydrogen and carbon penetration of the scale might be considered equally probable. In this case, $\alpha/\beta = 1$ and the same a_C value is arrived at for both gases. The wet gas case is considered further when discussing carburisation of Fe–9Cr.

Dilute Fe–Cr alloys reacted with CO_2–H_2O mixtures form multilayered, Fe-rich oxide scales. The layer in contact with the metal consists of an FeO + $(Fe,Cr)_3O_4$ mixture. Calculated "log p_{O_2}-composition" diagrams in the Fe–Cr–O system have been published for 627 °C [16] and 900 °C [17], and indicate that the equilibrium p_{O_2} at the interface between such a mixture and the underlying alloy is the dissociation pressure of FeO on pure iron. In fact, p_{O_2} at the triple point α-(Fe,Cr)/FeO/$(Fe,Cr)_3O_4$ is slightly lower than the dissociation pressure of FeO on pure Fe, because dissolution of chromium in FeO stabilises the latter. However, this effect is neglected here and the p_{O_2} associated with the equilibrium

$$(1-\delta)Fe + \frac{1}{2}O_2 = Fe_{1-\delta}O \tag{12}$$

is used to calculate the value of b for dilute alloys. Use of the equilibrium relationship

$$K_{12} = \frac{1}{(p_{O_2})_{eq}^{1/2}} \tag{13}$$

yields $b = K_2 K_{12}$. The value of K_{12} is calculated for $\delta = 0.053$ from data tabulated in Ref. [12].

High chromium alloys form Cr_2O_3 according to

$$\frac{2}{3}\underline{Cr} + \frac{1}{2}O_2 = \frac{1}{3}Cr_2O_3 \tag{14}$$

where $\underline{Cr}$ denotes chromium dissolved in the α matrix, with, at equilibrium,

$$K_{14} = \frac{1}{a_{Cr}^{2/3}(p_{O_2})_{eq}^{1/2}} \tag{15}$$

In this case, $b = K_2 K_{14} a_{Cr}^{2/3}$.

The validity of the proposed model is now tested against experimental results. Attention is focused on the behaviour of the Fe–9Cr alloy, for which the experimental data are most complete. Values of a_C calculated from Eq. (11) and thermochemical data tabulated in Ref. [12] are plotted in Fig. 15, along with a predominance diagram for Fe–9Cr. Phase boundaries in the Fe–9Cr–C system were calculated with the Thermo–Calc software and the TCFE4 database [18].

4.2. Carburisation at 650 °C

4.2.1. Fe–9Cr

According to the proposed model, Eq. (11) predicts carbon activities at the scale/alloy interface of oxidised alloys. However, the Fe–9Cr alloy produces both internal oxides and internal carbides, and the carburisation zone is not in contact with the scale/alloy interface (Fig. 5). Thus, predicted and experimental results apply to two distinct locations. In addition, the width of the carburisation zone is, a priori, affected by the inward movement of the oxidation front. Under certain conditions, the formalism developed by Meijering [10,19] to describe the simultaneous internal attack of dilute alloys by two oxidants may be used to overcome these difficulties.

The reaction morphology and schematic concentration profiles are depicted in Fig. 16. The two internal reaction zones are defined by the thermodynamic stability of the precipitates and the concentration of the oxidants. Essentially, as carbon diffusion in the metal is rapid, and carbon cannot react with the more stable chromium-rich oxide, the carbon concentration N_C does not decrease significantly across the oxide precipitation zone. Thus, the value of a_C calculated for the scale/alloy interface can to a good approximation be applied at the internal oxide/internal carbide interface. Furthermore, as the internal oxidation front advances, carbides are converted into oxides, and the carbon thus released diffuses inward to react with chromium at the carburisation front. Consequently, if the conversion is complete, the carburisation depth X_C can be defined from the interface between the internal oxidation and carburisation zones. In Fig. 12b, the TEM–EDS profile shows that the internal oxidation zone contains no carbon, and that the two

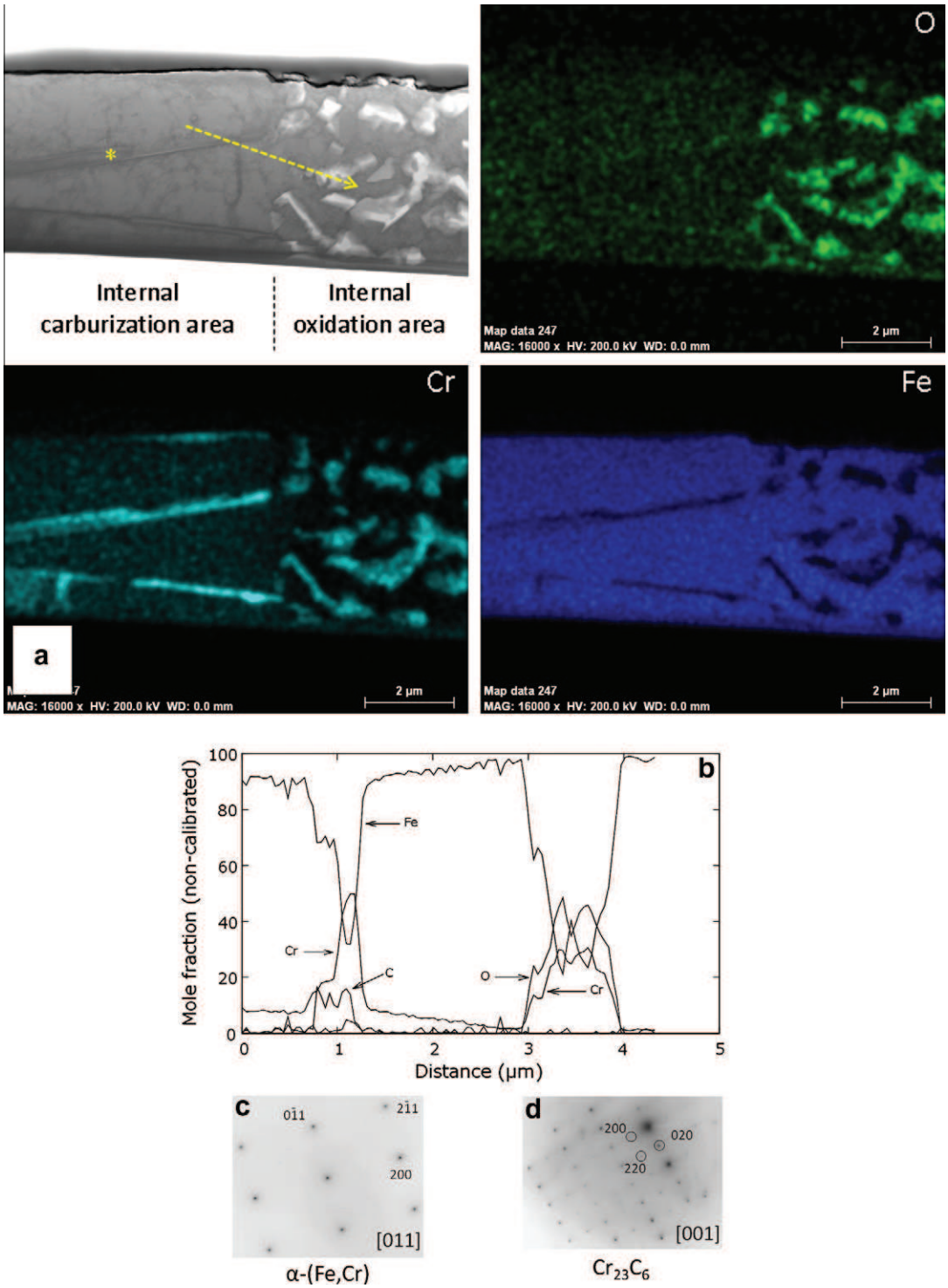

Fig. 12. TEM analyses at the interface between internal oxidation and carburisation areas in Fe–9Cr after 20 h exposure to Ar–20CO_2 at 800 °C. (a) Bright field image and corresponding EDS elemental maps; (b) EDS linescan; (c) and (d) selected area diffraction pattern of the α matrix ([011] zone axis) and of a $(Cr,Fe)_{23}C_6$ carbide ([0 0 1] zone axis), respectively. The arrow and star in (a) indicate the location of the linescan in (b) and of the pattern in (d), respectively.

precipitation zones are indeed distinct. That result was obtained after reaction at 800 °C, but is assumed also to apply at 650 °C.

The carbon activity predicted from equilibrium at the Fe–9Cr alloy/scale interface is seen in Fig. 15 to exceed the value required to form M_7C_3 at 650 °C, thus qualitatively accounting for the observed carburisation. The quantitative success of the model is now tested by examining the amount of carbide formed.

Provided that local thermodynamic equilibrium is achieved throughout the carburisation zone, a diffusion path on the phase diagram can be used to define the compositions of coexisting phases and their mass fractions, f_m. Mass and volume fractions are related through the densities of the phases (Table 2). Fig. 8 shows that in both gases, the carbide volume fraction decreases with increasing relative depth, according to a profile which is

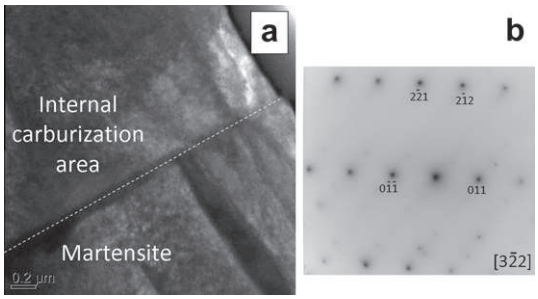

Fig. 13. TEM analyses at the interface between internal carburisation area and martensite in Fe–9Cr after 20 h exposure to Ar–20CO_2 at 800 °C. (a) Bright field image; (b) selected area diffraction pattern of martensite, showing characteristic (2$\bar{2}$1) and (2$\bar{1}$2) reflexions in the [3$\bar{2}\bar{2}$] zone axis.

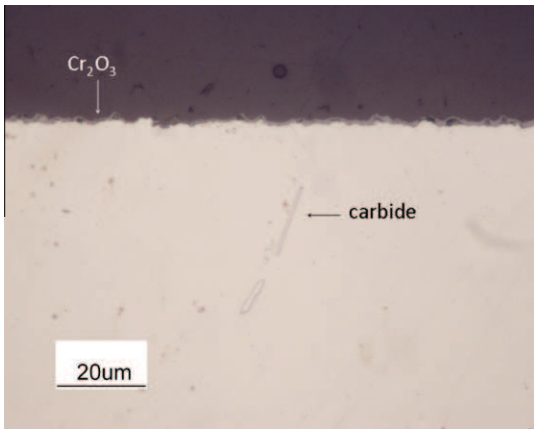

Fig. 14. Internal precipitation in Fe–20Cr after 100 h exposure to Ar–20CO_2 at 800 °C, etched with Murakami's reagent.

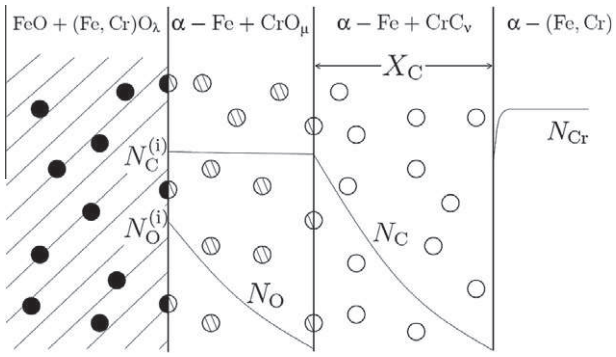

Fig. 16. Diffusion profiles during simultaneous reactions of oxygen and carbon with a dilute Fe–Cr alloy [10].

Table 2
Density of α-Fe and Cr carbides.

	ρ (g cm^{-3})	References
α-Fe	7.87	[20]
Cr_7C_3	6.92	[21]
$Cr_{23}C_6$	6.97	[21]

independent of reaction time. The steady-state distribution of phases within the precipitation zone supports the hypothesis of local thermodynamic equilibrium. Accordingly, the Fe–Cr–C phase diagram shown in Fig. 17 was constructed using Thermo–Calc. In this isothermal section, the points M, A and B represent the composition of the global system, the carbide precipitates and the metal matrix, respectively.

At 650 °C, the diffusion coefficients D_C [22,23] and D_{Cr} [24] in α-Fe are estimated as 2.4×10^{-7} and 5.6×10^{-14} cm^2 s^{-1}, respectively. Since $D_C \gg D_{Cr}$, chromium is assumed not to diffuse on a macroscopic scale, and the diffusion path lies along the dotted line in Fig. 17a. This path cuts tie-lines at points corresponding to different f_m values. Expressed in terms of volume fraction, f_V, these

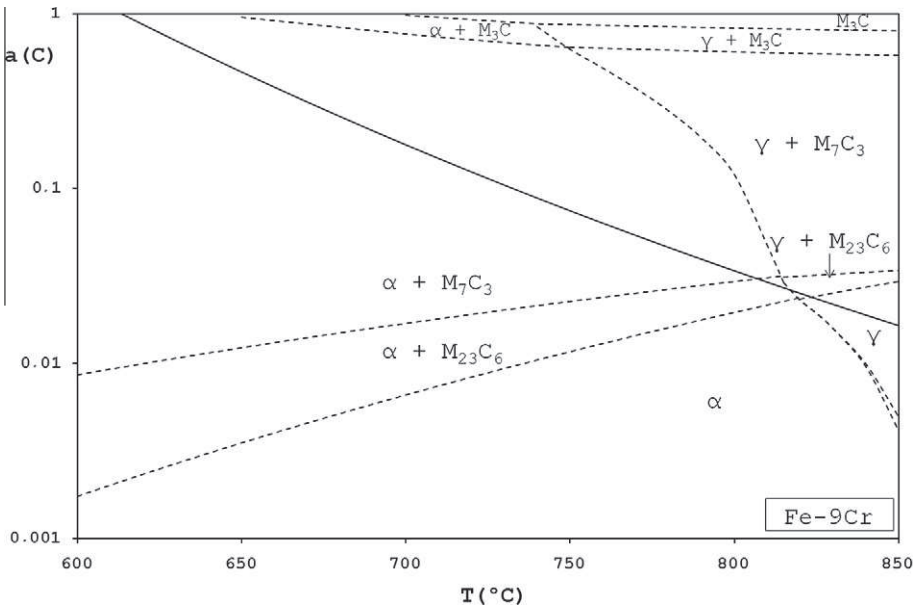

Fig. 15. Interfacial carbon activity from Eq. (11) (solid line) and predominance diagram from data in Thermo–Calc for Fe–9Cr (dashed lines).

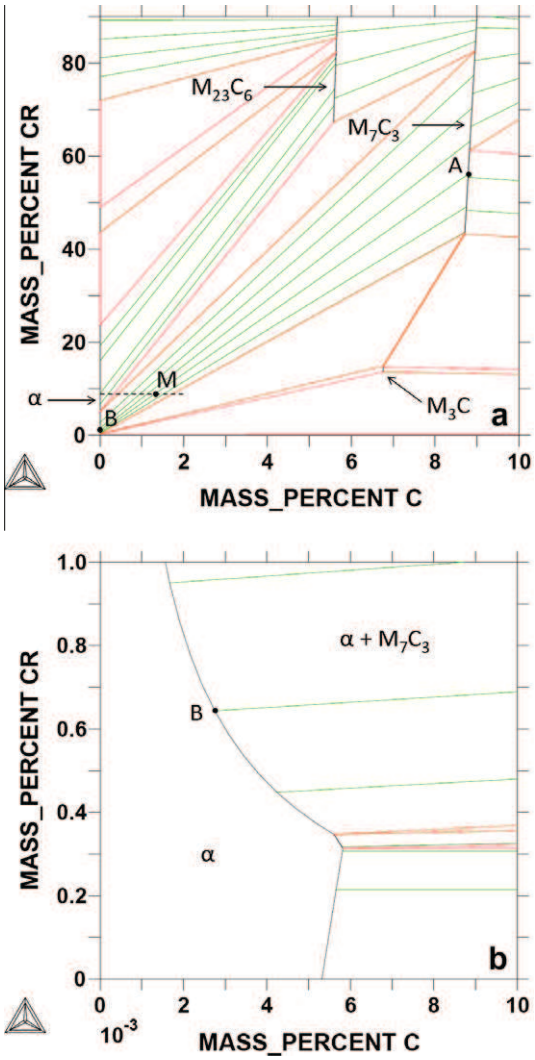

Fig. 17. Isothermal section of the Fe–Cr–C phase diagram at 650 °C. (a) Overall view; (b) Fe-rich corner. Points A, B and M are defined in text.

range from 0 to 0.07 in the $\alpha + M_{23}C_6$ field and from 0.06 to 0.2 in the $\alpha + M_7C_3$ field. Experimental f_V values, shown in Fig. 8, thus indicate that the near interface region corresponds to M_7C_3 precipitation in ferrite, and the deeper region to $\alpha + M_{23}C_6$. Measured volume fractions and XRD data (Fig. 6) are consistent and in agreement with the predicted reaction products.

Using the lever rule, a tie-line in the $\alpha + M_7C_3$ field corresponding to the volume fraction measured at the interface between internal oxidation and carburisation zones is selected. This defines the carbon content of the metal matrix $N_C^{(i)}$. Thermodynamic data for the dissolution of carbon in α-(Fe,Cr), obtained from Thermo-Calc, are then used to calculate the local equilibrium carbon activity. The amount of carbide formed during reaction with $Ar–20CO_2$ is found in this way to correspond to $a_C = 0.43$. In the case of reaction with $Ar–20CO_2–20H_2O$, the value $a_C = 0.21$ is obtained. These values are to be compared with that calculated from scale-alloy equilibrium (Eq. (11)) as 0.47. This good agreement provides support for the validity of the proposed model.

Further confirmation is available from the carburisation rates. The observed parabolic kinetics (Fig. 7) indicate diffusion control, and the rate constant k_p is related to carbon permeability according to Wagner's equation [25]

$$k_p = \frac{N_C^{(s)} D_C}{\nu N_{Cr}^{(0)}} \qquad (16)$$

where $N_C^{(s)}$ is the surface concentration of carbon in the metal matrix, ν the C/Cr ratio in the carbides, and $N_{Cr}^{(0)}$ the initial Cr mole fraction in the alloy. Diffusional blocking by the small equiaxed precipitates is ignored. In the presence of an external oxide scale, the surface concentration of carbon, $N_C^{(s)}$, is replaced by the interfacial value, $N_C^{(i)}$. For Eq. (16) to hold, (i) the condition $N_C^{(i)} D_C \gg N_{Cr}^{(0)} D_{Cr}$ must be met, (ii) carbon must react with chromium but not iron, and (iii) the carbides must be sufficiently stable for both chromium and carbon concentrations in the metal matrix to be negligible throughout the precipitation zone. These conditions are now examined in light of the volume fraction measurements presented in Fig. 8.

Using an average value of 0.15 for f_V at $x = 0$ and the phase diagram of Fig. 17 yields $N_C^{(i)} = 8.6 \times 10^{-5}$. The carbon permeability is then calculated from D_C values in α-Fe [22,23] as $N_C^{(i)} D_C = 4.0 \times 10^{-11}$ cm^2 s^{-1}. Standard data for D_{Cr} [24] lead to $N_{Cr}^{(0)} D_{Cr} = 5.4 \times 10^{-15}$ cm^2 s^{-1}, and the condition $N_C^{(i)} D_C \gg N_{Cr}^{(0)} D_{Cr}$ is satisfied.

Volume fraction profiles together with the phase diagram indicate that both M_7C_3 carbides in the near-surface precipitation zone, and $M_{23}C_6$ carbides deeper in the alloy, contain large amounts of iron. Values of N_C range from 1.3×10^{-4} at $x = 0$ to 9.4×10^{-6} at $x = X_C$, while N_{Cr} ranges from 6.6×10^{-3} at $x = 0$ to 8.3×10^{-2} at $x = X_C$. The latter values are not negligible. Thus the conditions of pure chromium carbide formation and complete chromium precipitation are not met. Consequently Wagner's simplified Eq. (16), whilst providing good order of magnitude prediction of k_p, lacks the accuracy required for present purposes.

The present situation of partial precipitation is described by Ohriner and Morral [26], applying the lever rule to the matrix-precipitate two-phase field to more accurately reflect the mass balance underlying Eq. (16). This procedure has been combined here with a numerical treatment of varying precipitate composition (defined in the phase diagram from f_V profiles), allowing $N_C^{(i)} D_C$ to be evaluated from k_p. Independently determined values of D_C [22,23] then allow calculation of $N_C^{(i)}$. The corresponding carbon activities are shown in Table 3, together with the values obtained from volume fraction measurements and those calculated from Eq. (11). Order of magnitude agreement between values obtained from the carburisation rates and those calculated for scale-alloy equilibrium further supports the validity of the thermodynamic model.

Estimates of a_C arrived at from measurements of carburisation extent and rate are consistently lower than predicted from the local equilibrium model (Table 3). This may represent a systematic failure to image all carbide precipitates metallographically. The discrepancy is even larger in the case of reaction with wet gas. This can be understood in terms of preferential uptake and/or transport of H-bearing molecules over C-bearing species. The extent of hydrogen enrichment can be estimated from Eq. (11), assuming again that $p_T = 0.4$ atm. Comparison of the a_C values determined for dry and wet gases (Table 3) yields $(p_{H_2} + p_{H_2O})/(p_{CO} + p_{CO_2}) = 6.2$ and 3.1, for the k_p and f_V calculations, respectively. The conclusion that selective uptake of H-bearing species decreases carbon penetration of an oxide is in agreement with earlier suggestions [1,9,27].

4.2.2. Fe–2.25Cr

Exposure of the Fe–2.25Cr alloy to dry CO_2 at 650 °C led to intergranular carburisation, but no intragranular carbides were observed (Fig. 4). Eq. (11) yields $a_C = 0.47$, which exceeds the value of 5.5×10^{-2} required to form M_7C_3 carbides in a Fe–2.25Cr alloy. The driving force for carbide precipitation in this alloy is less than in Fe–9Cr, where a value of 1.2×10^{-2} is sufficient to stabilise M_7C_3. The relatively low carbon supersaturation with respect to carbide formation is evident in preferential precipitate nucleation at grain boundaries. The qualitative implication of intergranular

Table 3
Carbon activity at the scale/alloy interface for the Fe–9Cr and Fe–20Cr alloys reacted at 650 °C.

Alloy	Gas	Experimental		Thermodynamic
		From k_p	From f_V	Equilibrium
Fe–9Cr	Ar–20CO_2	0.25	0.43	0.47
	Ar–20CO_2–20H_2O	0.07	0.21	
Fe–20Cr	Both	0.01	0.1	

carburisation is nonetheless clear. Carbon enrichment at the metal/oxide interface relative to the gas has occurred, in agreement with the model.

4.2.3. Fe–20Cr

The Fe–20Cr alloy produced a non-uniform reaction pattern at 650 °C, as illustrated by Fig. 3a. The cases of Cr_2O_3 scaling and of iron-rich oxide growth are discussed separately.

Since the dissociation pressure of Cr_2O_3 is extremely low, a very high carbon activity is expected from thermodynamic equilibrium at the Cr_2O_3/alloy interface. Values calculated from Eq. (11) exceed 10^4 in both gases. However, no graphite was observed, and carburisation occurred at a relatively low rate (Fig. 9a). This indicates a low interfacial carbon activity. Thus while carburisation did indeed occur beneath the Cr_2O_3 scale, the predicted carbon activity was not achieved. The assumption that CO_2 and CO access the metal/oxide interface at a sufficient rate for reaction (2) to reach equilibrium, and for Eq. (8) to be satisfied, is incorrect in this case. It is therefore concluded that transport of carbonaceous species through Cr_2O_3 is much slower than in iron oxide, as has already been suggested [4].

In regions beneath an iron-rich oxide scale, carburisation rates were similar in reactions in dry and wet CO_2 (Fig. 10). Average values of $k_p = 8 \times 10^{-11}$ cm^2 s^{-1} and $f_V = 0.3$ are used to calculate the carbon activities shown in Table 3, using the procedure described for the Fe–9Cr alloy. The values are lower than those predicted by Eq. (11). The low a_C values corresponding to the amount and rate of carburisation indicate that some degree of protection was obtained, even in locations where an iron-rich oxide scale had developed.

The value estimated via Eq. (16) from carburisation rates is likely to be in error. Non-uniform carburisation depths indicate that the onset of carburisation, which would correspond to breakdown of the protective scale, varied from place to place. Thus the times associated with measured precipitation depths would be shorter than the exposure time, and carburisation rates underestimated. Protection against carburisation of the Fe–20Cr alloy at 650 °C was partial, and only transient.

4.3. Carburisation at 800 °C

4.3.1. Fe–9Cr

Carburisation of Fe–9Cr at 800 °C produced chromium-rich $M_{23}C_6$ precipitates and martensite. Fig. 15 shows that the a_C value predicted from scale-alloy equilibrium is sufficient to form $M_{23}C_6$, but too low to reach the $\gamma + M_7C_3$ phase field. Moreover, no single-phase austenite field is available at this temperature, and the observed formation of martensite cannot be accounted for on this basis.

At 800 °C, chromium diffusion is significant, and subsurface alloy depletion could result from selective oxidation. Reference to the Fe–Cr–C phase diagram at 800 °C (not shown) indicates that single-phase austenite can form by carbon diffusion into chromium-depleted alloy. However, the minimum value of a_C required to form austenite in chromium-depleted alloy is of order 0.1, which exceeds the maximum value of $a_C = 3.4 \times 10^{-2}$ calculated for FeO–alloy equilibrium (Eq. (11)). This apparent conflict could be rationalised by proposing that preferential oxidation of chromium had occurred locally. Not only would this produce chromium-depleted metal capable of forming single-phase austenite when carburised, but also a chromium-rich oxide at the alloy surface, with a consequently lower oxygen activity and elevated a_C value.

The very irregular pattern of subsurface carburisation evident in Fig. 11 is certainly consistent with local variations in the scale/alloy interface conditions. However, the additional observation of isolated martensite within the alloy interior cannot be accounted for in this way. What is needed is a determination of chromium and carbon concentration profiles throughout the reacted zones. Nonetheless, formation of martensite and carbides beneath the oxide scale clearly demonstrates that carbon supersaturation was established at the metal/oxide interface, relative to the gas.

4.3.2. Fe–2.25Cr

No carburisation product was observed in the Fe–2.25Cr alloy after reaction at 800 °C. This is in agreement with the proposed model, since Eq. (11) predicts a carbon activity of 3.4×10^{-2}, below that required to form austenite (0.15) or M_7C_3 carbides (0.34).

4.3.3. Fe–20Cr

As discussed for reactions at 650 °C, Eq. (11) results in very high carbon activities below Cr_2O_3 scales, provided that they transmit the CO_2 and CO species. The very occasional presence of internal carbides after reaction at 800 °C suggests that the oxide was, in general, impervious to CO_2 and CO, but that microscopic failure occurred locally.

5. Summary and conclusions

Binary Fe–Cr alloys exposed to dry and wet CO_2 at 650 and 800 °C form external oxide scales. Despite the very low gas phase carbon potentials, the alloys generally sustain carburisation attack beneath their oxide scales.

Carbon activities required to form the observed reaction products are calculated from thermodynamic data, and shown to exceed gas phase equilibrium values by factors of about 10^{12} to 10^{13}.

A local equilibrium model is used to relate carbon and oxygen activities via the CO_2 and H_2O dissociation and Boudouard reactions. Application of this description to the scale/alloy interface, where the oxygen potential is low, leads to the prediction of carbon activity values high enough to form chromium-rich carbides.

Quantitative testing of the model was performed in the case of Fe–9Cr reaction at 650 °C. Measured amounts of carbide precipitated at the scale/alloy interface are shown to agree well with the thermodynamically predicted value of $a_C = 0.47$.

Parabolic carbide precipitation kinetics indicate diffusion control. Rate constants measured for Fe–9Cr at 650 °C provide an additional means of estimating interface carbon activities. The results reinforce the conclusion that carbon activities are controlled by scale–alloy equilibrium.

Carburisation of Fe–9Cr also occurs at 800 °C, producing martensite and chromium-rich carbides. However, the reaction did not achieve a steady state condition in the times examined.

Carbon activities in Fe–Cr alloys beneath external oxide scales are elevated far above ambient gas phase values, provided that carbon can penetrate the scale. The mobile species has not been identified, but is modelled successfully as $CO–CO_2$. The presence of water vapour lowers the carbon activity, probably by partially excluding the carbonaceous species from the scale. A chromia scale provides a more effective barrier to carbon than does an iron-rich oxide.

Acknowledgements

The authors acknowledge access to the UNSW node of the Australian Microscopy and Microanalysis Research Facility (AMMRF), and thank Electron Microscope Unit staff for help with TEM analyses. Financial support from the Australian Research Council Discovery program is gratefully acknowledged.

References

[1] J. Pirón Abellán, T. Olszewski, H.J. Penkalla, G.H. Meier, L. Singheiser, W.J. Quadakkers, Scale formation mechanisms of martensitic steels in high CO_2/H_2O-containing gases simulating oxyfuel environments, Mater. High Temp. 26 (2009) 63–72.
[2] G.H. Meier, K. Jung, N. Mu, N. Yanar, F. Pettit, J. Pirón Abellán, T. Olszewski, L. Nieto Hierro, W.J. Quadakkers, G.R. Holcomb, Effect of alloy composition and exposure conditions on the selective oxidation behavior of ferritic Fe–Cr and Fe–Cr–X alloys, Oxid. Met. 74 (2010) 319–340.
[3] H.E. McCoy, Type 304 stainless steel vs flowing CO_2 at atmospheric pressure and 1100–1800F, Corrosion 21 (1965) 84–94.
[4] C.S. Giggins, F.S. Pettit, Corrosion of metals and alloys in mixed gas environments at elevated temperatures, Oxid. Met. 14 (1980) 363–413.
[5] C.T. Fujii, R.A. Meussner, Carburization of Fe–Cr alloys during oxidation in dry carbon dioxide, J. Electrochem. Soc. 114 (1967) 435–442.
[6] I. Wolf, H.J. Grabke, A study on the solubility and distribution of carbon in oxides, Solid State Commun. 54 (1985) 5–10.
[7] X.G. Zheng, D.J. Young, High-temperature corrosion of Cr_2O_3-forming alloys in $CO–CO_2–N_2$ atmospheres, Oxid. Met. 42 (1994) 163–190.
[8] X.G. Zheng, D.J. Young, High temperature corrosion of pure chromium in $CO–CO_2–SO_2–N_2$ atmospheres, Corros. Sci. 36 (1994) 1999–2015.
[9] D.J. Young, Simultaneous oxidation and carburisation of chromia forming alloys, Int. J. Hydrogen Energy 32 (2007) 3763–3769.
[10] D.J. Young, High temperature oxidation and corrosion of metals, Elsevier, Amsterdam, 2008.
[11] N. Birks, in: Z.A. Foroulis, F.S. Pettit (Eds.), Corrosion of High Temperature Alloys in Multicomponent Oxidative Environments. Electrochem. Soc., Las Vegas, 1976, pp. 215–260.
[12] I. Barin, Thermochemical Data of Pure Substances, second ed., VCH, Weinheim, 1993.
[13] M.R. Taylor, J.M. Calvert, D.G. Lees, D.B. Meadowcroft, The mechanism of corrosion of Fe–9%Cr alloys in carbon dioxide, Oxid. Met. 14 (1980) 499–516.
[14] A.M. Pritchard, N.E.W. Hartley, J.F. Singleton, A.E. Truswell, Oxygen-18 and deuterium profiling in thick films on Fe–9%Cr alloys by 3 MeV nuclear microprobe, Corros. Sci. 20 (1980) 1–17.
[15] C. Boudias, D. Monceau, 1989–2010, <http://carine.crystallography.pagespro-orange.fr/>, date accessed (2010).
[16] H. Davies, A. Dinsdale, Theoretical study of steam grown oxides as a function of temperature, pressure and $p(O_2)$, Mater. High Temp. 22 (2005) 15–25.
[17] A.D. Pelton, H. Schmalzried, J. Sticher, Computer-assisted analysis and calculation of phase diagrams of the Fe–Cr–O, Fe–Ni–O and Cr–Ni–O systems, J. Phys. Chem. Solids 40 (1979) 1103–1122.
[18] B. Sundman, B. Jansson, J.O. Andersson, The Thermo–Calc databank system, CALPHAD: Comput. Coupling Phase Diagrams Thermochem. 9 (1985) 153–190.
[19] J.L. Meijering, in: H. Herman (Ed.), Advances in Materials Research, Wiley-Interscience, New York, 1971, pp. 1–81.
[20] Physical Constants of Inorganic Compounds, in: W.M. Haynes (ed.), CRC Handbook of Chemistry and Physics, 91st Edition, CRC Press/Taylor and Francis, Boca Raton, 2010, pp. 4/43–4/101.
[21] H.J. Goldschmidt, Interstitial Alloys, Butterworths, London, 1967.
[22] E. Budke, C. Herzig, H. Wever, Volume and grain-boundary diffusion of ^{14}C in α-Fe, Phys. Status Solidi A 127 (1991) 87–101.
[23] K. Tapasa, A.V. Barashev, D.J. Bacon, Y.N. Osetsky, Computer simulation of carbon diffusion and vacancy-carbon interaction in α-iron, Acta Mater. 55 (2007) 1–11.
[24] A.W. Bowen, G.M. Leak, Solute diffusion in alpha- and gamma-iron, Metal. Trans. 1 (1970) 1695–1700.
[25] C. Wagner, Reaktionstypen bei der Oxydation von Legierungen, Zeit. Elektrochem. 63 (1959) 772–790.
[26] E.K. Ohriner, J.E. Morral, Precipitate distribution in subscales, Scr. Metal. 13 (1979) 7–10.
[27] D.J. Young, Effects of water vapour on the oxidation of chromia formers, in: P. Steinmetz, I. Wright, A. Galerie, D. Monceau, S. Mathieu (Eds.), 7th International Symposium on High Temperature Corrosion and Protection of Materials, vol. 595-598, Les Embiez, France, pp. 1189–1197.